Short-scale variations in high-resolution crystal-preferred orientation data in an alpine ice core – do we need a new statistical approach?

Johanna Kerch[1,2*], Olaf Eisen[1,3], Jan Eichler[1], Tobias Binder[1], Johannes Freitag[1], Pascal Bohleber[2,4†], Paul Bons[5], Ilka Weikusat[1,5]

[1]Alfred Wegener Institute Helmholtz Centre for Polar and Marine Research, 27568 Bremerhaven, Germany
[2]Institute of Environmental Physics, Heidelberg University, 69120 Heidelberg, Germany
[3]Department of Geosciences, University of Bremen, Bremen, Germany
[4]Institute for Interdisciplinary Mountain Research, Austrian Academy of Sciences, Innsbruck, Austria
[5]Department of Geosciences, Eberhard-Karls-University Tübingen, 72074 Tübingen, Germany

Key Points:

- Crystal-preferred orientation data were collected in high-resolution in intervals of up to 1 m length in a cold Alpine ice core.
- A strong anisotropy and high spatial variability on the cm-scale is found and challenges established practices in fabric sampling.
- Strain localisation is considered as main driver of short-scale variations in crystal-orientation fabric in ice.

*Currently: Georg-August-University Göttingen, Department of Physics, Friedrich-Hund-Platz 1, 37077 Göttingen, Germany
†Now at: University Ca' Foscari of Venice, Dept. Environmental Sciences, Informatics and Statistics, Via Torino 155, 30172 Venezia Mestre, Italy

Corresponding author: Johanna Kerch, johanna.kerch@awi.de

Corresponding author: Ilka Weikusat, ilka.weikusat@awi.de

Abstract

We analysed crystal-preferred orientation of c-axis and microstructure data from the Alpine ice core KCC at an unprecedented resolution and coverage of any Alpine ice core. We find that an anisotropic single-maximum fabric develops as early as 25 m depth in firn under vertical compression and strengthens under simple shear conditions towards the bedrock at 72 m depth. The analysis of continuously measured intervals with subsequent thin section samples from several depths of the ice core reveals a high spatial variability in the crystal orientation and crystal size on the 10 cm-scale as well as within a few centimeters. We quantify the variability and investigate the possible causes and links to other microstructural properties. Our findings support the hypothesis that the observed variability is a consequence of strain localisation on small spatial scales with influence on fabric and microstructure. From a methodological perspective, the results of this study lead us to challenge whether single thin sections from ice cores provide representative parameters for their depth to be used to infer the fabric development in a glacier on the large scale. Previously proposed uncertainty estimates for fabric and grain size parameters do not capture the observed variability. This might therefore demand a new scale-sensitive statistical approach.

1 Introduction

One of the foremost goals of contemporary glaciological research is to advance our understanding of the internal deformation of glaciers and ice sheets to better constrain the dynamic components of modelled projections of their development under changing climate conditions. To this end, the physical properties of polycrystalline glacier ice have been studied on a number of deep ice cores from the polar regions for more than 40 years, as reviewed in Faria, Weikusat, and Azuma (2014a). The analysis of crystal-preferred orientation (CPO, fabric) and microstructure (μS) on ice core samples provides evidence to draw conclusions on dominant deformation and recrystallisation (RX) regimes at different depths in the ice column (Weikusat, Jansen, et al., 2017), and may also be of importance for the interpretation of climate records (Faria, Freitag, & Kipfstuhl, 2010; Kennedy, Pettit, & DiPrinzio, 2013). To clarify the terminology in this study, *microstructure* includes the shape and size of grains, grain boundaries (GBs), bubbles and other spatial features in ice, while *fabric* is only used for crystallographic orientation of crystals.

The inherent plastic anisotropy of individual ice crystals (Duval, Ashby, & Anderman, 1983) leads to their alignment in preferred orientations under the local stress conditions along the flow path (Azuma & Higashi, 1985). Dynamic recrystallisation occurs as a consequence of the accumulated strain energy (Llorens et al., 2017; Schulson & Duval, 2009), and the presence of pore space and impurities contribute to the complex development of fabric and microstructure (Azuma, Miyakoshi, Yokoyama, & Takata, 2012; Durand, Weiss, et al., 2006; Eichler et al., 2017; Steinbach et al., 2016). As a result of these inter-dependent micro-scale processes, the viscous behaviour of the ice bulk is changing, which, in turn, can lead to an enhancing feedback on the deformation (Azuma & Goto-Azuma, 1996). To establish a thorough understanding of how dynamic processes on the micro-scale, recorded as a temporal snapshot in ice-core data, are connected with the observations on the macro-scale, remains a major challenge in the study of ice-physical properties (Eisen, Hamann, Kipfstuhl, Steinhage, & Wilhelms, 2007).

While it has repeatedly been demonstrated that it is essential to include the crystal anisotropy into ice flow models (Graham, Morlighem, Warner, & Treverrow, 2018; Martin, Gudmundsson, Pritchard, & Gagliardini, 2009; Pettit, Thorsteinsson, Jacobson, & Waddington, 2007; Seddik, Greve, Placidi, Hamann, & Gagliardini, 2008), it is difficult to obtain the necessary amount of data from an ice core which is representative for the CPO development in the vertical dimension, while the sampling in the horizontal dimension is, in any case, limited to the cross-section of the core. In fact, it is currently not constrained how much ice-core data can be considered as representative. Due to the time-consuming nature of fabric studies, sampling for this purpose is typically in

the order of one sample per tens of metres of ice core. Sampling is thus at a very low resolution with much less than a few per cent of the core analysed. (appendix A, Table A.1). Despite this, the results are assumed to reflect the general fabric evolution in the ice column. However, some studies report the observation of small-scale features like fine-grained layers in the microstructure and sudden spatial changes between distinct fabric patterns on a resolution of about 15 m (DiPrinzio et al., 2005; Fitzpatrick et al., 2014; Jansen et al., 2016; Montagnat et al., 2014). It stands to question if these structures are common to most ice cores, potentially (1) distorting the perceived representation from low-resolution ice-core fabric studies, and (2) disregarding information on deformation processes on smaller scales.

Only a few studies are focused on the fabric of non-polar (e.g. alpine or sub-polar) glacier ice, with most of them being older than 30 years and/or from temperate glaciers (Table 1; see also the review paper from Hudleston, 2015). While the measurement techniques were certainly less sophisticated in the past, and these thus provided statistically less representative data sets, it was reported that samples from nearby locations (within a few meters) showed distinctly different fabric (Kamb, 1959; Rigsby, 1951) and bands with small crystals and single-maximum fabrics were observed in an ice core (Vallon, Petit, & Fabre, 1976). Non-polar glaciers offer the opportunity to study glaciological processes that can be assumed to follow the same physical laws as in polar regions, on a smaller spatial scale and a more constrained temporal scale, providing upper limits for the duration of microstructural processes. The ice temperature is generally higher compared to the non-basal parts of polar ice sheets and often similar to the temperatures encountered at the base of polar ice sheets, approaching the pressure-melting point, where temperature-driven microstructural processes may be enhanced (Faria, Weikusat, & Azuma, 2014b). They can thus serve as in-situ or natural laboratories with deformation conditions that are not feasible in laboratory experiments and several orders closer to those in polar ice sheets. However, the majority of non-polar ice cores from the last 30 years were analysed with a climatological focus (e.g. Bohleber, Wagenbach, Schner, & Bhm, 2013; Preunkert, Wagenbach, Legrand, & Vincent, 2000; Schwikowski, Brütsch, Gäggeler, & Schotterer, 1999; Thompson et al., 2006). Only recently, some low-resolution fabric data from an ice core drilled in 1992 on the Tibetan Plateau (Thompson et al., 1995) were reported and compared to polar fabric data (Y. Li, Kipfstuhl, & Huang, 2017).

The cold high-Alpine glacier Colle Gnifetti (CG) has long been the subject of extensive glaciological research, with a focus on its archive of midlatitude climate (Wagenbach, Bohleber, & Preunkert, 2012). In the present study we provide the first comprehensive fabric analysis on this Alpine glacier, obtained from a recent ice core. For the first time, we systematically analyse the variability of fabric on a scale of centimeters to decimeters within continuously analysed depth intervals.

While the crystallographic evolution is the main focus of the study, other physical properties and microstructural parameters (grain size, density, bubbles) are considered for the benefit of discussing the context of physical processes that could influence the fabric development at Colle Gnifetti. Following the findings of our study, we discuss the significance of defining a representative scale length for fabric studies.

2 Study Site

The high-Alpine glacier Colle Gnifetti, Monte Rosa Massif, on the border between Switzerland and Italy, is characterized by a high spatio-temporal variability in net snow accumulation which is primarily a result of insolation-driven snow consolidation counteracting the effect of wind erosion (Wagenbach, Mnnich, Schotterer, & Oeschger, 1988). On average, net snow accumulation is mainly made up by precipitation during the warm seasons, with a minor but highly variable contribution by winter snow. The average net accumulation rate at KCC was determined around 22 cm water equivalent per year (Bohleber et al., 2018).

Table 1. Early and more recent crystallographic studies on non-polar or subpolar glaciers. We would like to mention current projects involving crystal-orientation measurements on temperate and polythermal ice on Rhone Glacier, Switzerland (Hellmann et al., 2018) and Storglaciären, Sweden (Monz & Hudleston, 2018), and Jarvis Glacier, Alaska (Gerbi et al., 2018). *Section* refers to a thin section sample.

Authors	Region	Type & Temperature	Fabric resolution; sample description
Rigsby (1951)	Emmons glacier, Mt. Rainier, Washington, USA	Mountain and valley glacier, temperate	11 surface locations, stagnant and fast flowing ice; $\sim$40 sections with 1725 crystals
Meier, Rigsby, and Sharp (1954)	Saskatchewan Glacier, Alberta, Canada	Valley glacier, temperate	8 surface locations
Rigsby (1960)	Emmons, Saskatchewan and Malaspina Glacier, Alaska, USA; Moltke Glacier and Nunatarssuak Ice Ramp, Thule, Greenland	3 temperate, 2 polar sites	surface locations, 8000 crystals
Kamb (1959), Allen, Kamb, Meier, and Sharp (1960)	Lower Blue Glacier, Washington, USA	Valley glacier, ablation zone, temperate	9 surface locations, 144 sections
Taylor (1963)	Burroughs Glacier, Alaska	Ablation zone, temperate	2 surface locations
Higashi (1967)	Mendenhall Glacier, Alaska	Temperate	30 samples
Jonsson (1970)	Isfallsglaciären (and Storglaciären), Sweden	Small valley glacier, ablation zone, polythermal	9 locations at glacier base (tunnel), oriented ice blocks, 81 sections
Hooke (1973)	Barnes ice cap, Baffin Island, Canada	Ice cap margin, cold ($-10\,^\circ$ C)	4 shallow ice cores and surface locations; 18 sampling sites in intervals of $\sim$5–10 m
Vallon et al. (1976)	Vallée Blanche, Mt. Blanc, France	Valley glacier, accumulation zone, 3550 m a.s.l., temperate	Ice core (30 m firn and 150 m ice); ca. 50 sections in intervals of $\sim$10 m
Hudleston (1980)	Barnes ice cap, Baffin Island, Canada		
Tison and Hubbard (2000)	Glacier de Tsanfleuron, Switzerland	Plateau glacier, 2400–2900 m a.s.l., temperate	8 ice cores (along-flow transect), 5 in the ablation zone, 3 in the accumulation zone without reaching bedrock, 170 m in total; 348 sections with 3000 crystals
Y. Li et al. (2017)	Guliya ice cap, Tibetan Plateau	Ice cap, 6200 m a.s.l., cold ($-2\,^\circ$ C)	Ice core, 309 m to bedrock; sampled $\sim$1 % in intervals of $\sim$10 m
This study	**Colle Gnifetti, Switzerland/Italy**	**Mountain glacier, 4484 m a.s.l., cold (below $-10\,^\circ$ C)**	**92 sections from 72 m ice core, 12% of glacier thickness sampled, $\sim$67000 crystals**

The most prominent studies showing fabric diagrams and giving microstructural quantities that could be found (and were accessible) in peer-reviewed literature in English are summarized here. We do not claim that this table is complete.

The ice core KCC was drilled to bedrock in 2013 (N 45° 55.736, E 7° 52.576, 4484 m a.s.l., Bohleber et al., 2018) in about 100 m distance to the ice core KCI, drilled in 2005 (Bohleber et al., 2013), on a flank towards an ice cliff. KCC is 72 m long and the firn-ice transition was found to be at a depth of about 36 m. A borehole temperature between −13.6 ° C in 13 m depth and −12.4 ° C at the bedrock was measured in 2014 (Hoelzle, Darms, Lthi, & Suter, 2011, no change since 2011, pers. comm. M. Hoelzle, University of Fribourg, 2014), implying that the ice is frozen to bedrock. Radiocarbon dating revealed a basal ice age of ∼4000 years BP from the ice core sections at bedrock (Hoffmann et al., 2017). Therefore, we can assume that ice from different depths of the core has experienced quite a different deformation history despite the ice core's short length. Surface velocities at Colle Gnifetti were last measured from 2014 to 2016 and were of the order of $1\,\mathrm{m\,a^{-1}}$ close to the KCC borehole (Licciulli, 2018).

3 Laboratory Measurements and Processing

The ice core was stored at −18 ° C during transport and at −30 ° C before and after processing. Vertical thin sections ($33 \times 100\,\mathrm{mm^2}$, ca. 300 μm thick) of the ice core were prepared with a standard microtoming procedure in 13 intervals between 25 m and 72 m depth. Over each interval they provide continuous records of up to 110 cm length in depth. *Continuous* refers to measurements of several adjacent sections in an ice core segment or bag. The azimuthal orientation of the sections may vary due to deliberate rotation of core segments during processing, which was noted and considered in the analysis, or accidental loss of orientation information during core logging. Crystallographic c-axis orientations were measured by means of polarized light microscopy (e.g. Heilbronner & Barrett, 2014; Peternell, Kohlmann, Wilson, Seiler, & Gleadow, 2009; Wilson, Russell-Head, & Sim, 2003) with an automatic fabric analyser from Russell-Head Instruments (FA, model G50). Additionally, microstructural maps (Kipfstuhl et al., 2006) were acquired with a Large Area Scanning Macroscope (LASM, Schäfter+Kirchhoff, Binder, Garbe, Wagenbach, Kipfstuhl, & Freitag, 2013) from the same section surface to obtain supporting information on pore space and grain boundaries. The KCC fabric data consist of 92 vertical thin sections and samples 12 % of the entire ice core.

For each pixel of the thin section the measurement provides the orientation of the crystallographic c-axis by two angles, azimuth ϑ in the interval $[0, 2\pi]$ and colatitude φ in the interval $[0, \pi/2]$, with respect to the (nearly) vertical ice-core axis. The c-axis is expressed as a vector $\vec{c}$ with unit length:

$$\vec{c}(\vartheta, \varphi) = (\sin(\varphi)\cos(\vartheta), \sin(\varphi)\sin(\vartheta), \cos(\varphi)). \tag{1}$$

The obtained FA data are processed using the open-source software `cAxes` developed at AWI (Eichler, 2013) for automatic pixel-wise image analysis, excluding pixels with quality below 50 % (Peternell et al., 2009) and setting a lower grain size threshold of $A_{\min} = 0.2\,\mathrm{mm^2}$ (constrained by the section thickness $> 200\,\mu$m).

Eigenvalues λ_i ($i = 1, 2, 3$; $\lambda_1 \leq \lambda_2 \leq \lambda_3$; $\sum \lambda_i = 1$) of the second-order orientation tensor $a_{ij}^{(2)}$ are calculated from the c-axis distribution of a thin section sample (Adam, 1989; Durand, Gagliardini, et al., 2006; Wallbrecher, 1986) and are weighted with the grains' cross-section area A as proposed and discussed by Gagliardini, Durand, and Wang (2004). These are standard parameters to classify the type and strength of the crystallographic-preferred orientation and can be associated with different deformation regimes (e.g. Weikusat, Jansen, et al., 2017). We can calculate a statistical uncertainty for the eigenvalues σ_λ depending on the sample size of the crystal ensemble N_g following Durand, Gagliardini, et al. (2006):

$$\sigma_\lambda = (-1.64\lambda^2 + 1.86\lambda - 0.14) N_\mathrm{g}^{-1/2}. \tag{2}$$

We remark that this equation will not give a positive uncertainty estimate below $\lambda = 0.081$. The uncertainty σ_A, which accounts for sectioning and population effects when calculating the mean grain size $\bar{A}$ as determined from the number of pixels per grain in

a 2-D section, is estimated by

$$\sigma_A = 2\bar{A}(0.02 + 0.44\, N_{\mathrm{g}}^{-1/2}). \tag{3}$$

However, this uncertainty is based on the assumption of regular grain features during normal grain growth (Anderson, Grest, & Srolovitz, 1989; Durand, Gagliardini, et al., 2006) which can no longer be assumed to be the dominant process as soon as RX processes set in (Faria et al., 2014b). The measurement uncertainty associated with the FA instrument was shown to be small enough to be neglected compared to the sampling uncertainty (Montagnat et al., 2012).

For the centimeter-scale analysis along the measured core segments we apply a sliding window frame of 2 cm height and 2 mm step size for the calculation of second-order orientation tensor eigenvalues and mean grain size. The median number of grains per window with area $33 \times 20\,\mathrm{mm}^2$ is 143 with an interquartile range of $90 - 217$.

Additionally, the high-resolution density profile for the upper 50 m of the ice core was determined by evaluating 2D projected X-ray computer tomography images (XCT, Freitag, Wilhelms, & Kipfstuhl, 2004). Visual stratigraphy images (Svensson et al., 2005) were recorded over the full length and qualitatively analysed with focus on the visibility of well-defined layers and layer inclination. The number density and size of closed-off bubbles in the ice was determined from the LASM images using the open-source software `ImageJ`. The records of dust-related impurities and stable water isotopes presented in Bohleber et al. (2018) were available for comparison with the crystal data (more extensively discussed in Kerch, 2016).

4 Results

4.1 Physical Properties Profile

We present the comprehensive data set from a classical thin section-scale fabric analysis, but from continuously measured intervals instead of just one thin section sample per interval. Figure 1 shows the depth profile of area-weighted second-order orientation tensor eigenvalues for KCC, the mean and maximum grain size per section and the high-resolution density from XCT. The uncertainties are calculated with Eq. 2 and 3. Additionally, the standard deviation of the grain size distribution is indicated towards higher grain sizes. Schmidt diagrams for individual thin sections are shown in appendix B, Fig. B.1.

The data reveal how a distinct anisotropy of c-axes evolves with depth. A weakly anisotropic fabric can already be observed in the firn. The crystal anisotropy quickly increases across the firn-ice transition down to 53 m, developing a broad single-maximum fabric. In the lower 20 m of the core a small portion of grains are forming a weak girdle pattern in combination with narrowing of the strong single maximum, with a minimum spherical aperture (cone angle) of 9° at the bedrock, and increasingly inclined to the vertical, with a maximum inclination angle of the c-axis eigenvector at bedrock of 27°.

Remarkable is the high variability of eigenvalues within continuously measured intervals, at all depths of the ice core, with the exception of the deepest 70 cm long interval close to bedrock. This variability exceeds the estimated population-dependent uncertainty and does not show a discernible trend. In the following, the c-axis eigenvalue $\lambda_3 e$ is considered as a single parameter to further investigate the small-scale fabric variability, as single-maximum fabric is recognized as the dominant fabric type. Table 2 lists the average c-axis eigenvalue and difference between extreme values for each interval. The difference exceeds 0.1 in most intervals.

The mean grain size $\bar{A}$ lies between $1\,\mathrm{mm}^2$ and $18\,\mathrm{mm}^2$ calculated from 155−1707 grains per section, with 75 % of the entire grain population smaller than $8\,\mathrm{mm}^2$. Note that for most sections 75 % of all grains are smaller than the calculated mean grain size. The grain size tends to increase from the firn towards a depth of approximately 48 m and subsequently shows a sharp decrease in the interval near the bedrock. However, the vari-

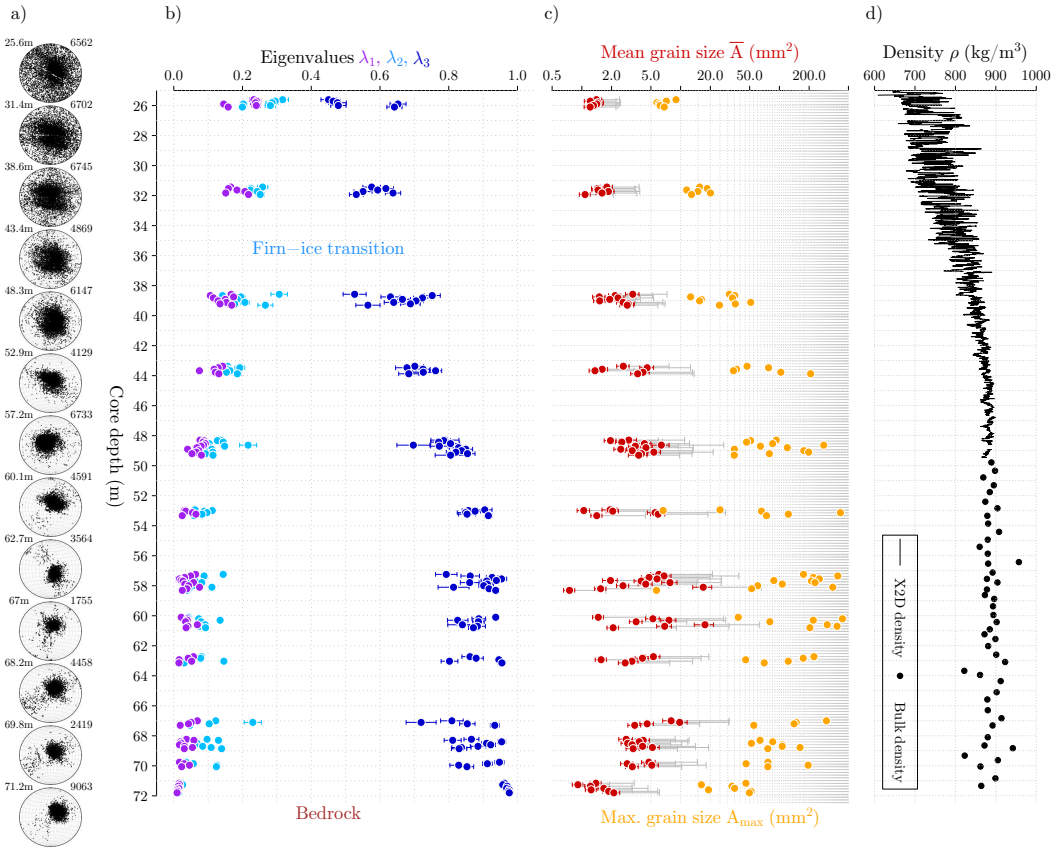

Figure 1. Evolution of a) c-axis distributions, b) c-axis orientation tensor eigenvalues (area-weighted), c) grain sizes and d) density with depth. Uncertainties $2\sigma_\lambda$ (blue) and $2\sigma_A$ (red) are calculated with Eq. 2 and 3. The standard deviation of the mean grain size (red) is additionally shown as grey whiskers (on a logarithmic scale). The maximum grain size is shown in orange. C-axis distributions are presented per continuously measured interval (Schmidt diagrams with the centre corresponding to the ice core axis). Each dot represents a single grain as identified from the thin section data. The top depth and number of grains are indicated on the top left/right of each pole figure. The azimuthal orientation of the Schmidt diagrams varies but could not be further constrained.

ability in mean grain size within an interval increases, in conjunction with a strong increase in the maximum grain size A_{max} up to 4 cm^2 in 48–68 m depth. The calculated uncertainty associated with the sectioning and population effect for calculating the mean grain size is much lower than the standard deviation.

4.2 Visual Stratigraphy

We identify six depth zones in which the characterisation of the visual stratigraphy changes (Table 3, Fig. B.3), considering the contrast between and the thickness of alternating lighter and darker bands in the visual stratigraphy linescan images. For most of the core a stratigraphic order can be observed, which, however, cannot be discerned in the images in the bottom 5 m. The layer inclination varies strongly in the firn and increases towards bedrock in the ice with maximum values of 30°. As we do not know the orientation of the ice core (and thus that of the image plane) with respect to the geographical coordinates and flow direction, layer inclination values can only be minimum

Table 2. Mean c-axis eigenvalues $\bar{\lambda}_3$ with standard deviation and variability for each interval (indicated by top depth and length) of continuous measurements, calculated on the thin section (Fig. 1) and cm-scale (Fig. 3).

Top depth (m)	Length (m)	Mean c-axis eigenvalue $\bar{\lambda}_3$ (thin section-scale)	Variability $\lambda_{3,\max} - \lambda_{3,\min}$ (thin section-scale)	Mean c-axis eigenvalue $\bar{\lambda}_3$ (cm-scale)	Variability $\lambda_{3,\max} - \lambda_{3,\min}$ (cm-scale)
25.61	0.59	0.53 ± 0.09	0.2	0.54 ± 0.12	0.48
31.43	0.6	0.58 ± 0.04	0.11	0.6 ± 0.06	0.31
38.58	0.79	0.66 ± 0.07	0.23	0.67 ± 0.08	0.4
43.37	0.6	0.71 ± 0.03	0.08	0.72 ± 0.06	0.25
48.3	1.04	0.8 ± 0.04	0.16	0.81 ± 0.07	0.34
52.94	0.49	0.88 ± 0.03	0.07	0.87 ± 0.04	0.19
57.24	1.14	0.89 ± 0.05	0.16	0.9 ± 0.05	0.21
60.1	0.8	0.88 ± 0.04	0.11	0.9 ± 0.05	0.21
62.73	0.51	0.89 ± 0.06	0.15	0.9 ± 0.07	0.3
67	0.4	0.83 ± 0.09	0.21	0.85 ± 0.10	0.45
68.23	0.72	0.88 ± 0.05	0.14	0.89 ± 0.06	0.25
69.76	0.4	0.89 ± 0.05	0.12	0.89 ± 0.05	0.17
71.16	0.71	0.97 ± 0.01	0.02	0.96 ± 0.01	0.05

estimates. Also, a possible borehole inclination during drilling might have an unquantifiable effect on the layer inclination. However, borehole inclination measurements from 2016 revealed inclination angles below 5° between 10 and 60 m depth and 5−10° down to bedrock (Licciulli, 2018). This is not sufficient to account for the observed layer inclination in the visual stratigraphy record and has probably mostly developed over 3 years since the drilling.

About 20 melt layers (thickness $\mathcal{O}$(cm)) were found in the firn part of the ice core, as is to be expected at this drilling site (Alean, Haeberli, & Schdler, 1983), often with coarse grains in the vicinity of the melt features.

On visual inspection of the thin section microstructure images, we assess how often we observe a distinct change in grain size in layers, regardless of the mean grain size in these layers. In more than a third of all sections we find such grain size layer transitions. Fine-grained layers (19 observations, Fig. 2) occur most frequently at depths between the firn-ice transition and 60 m. An estimated 17 % of all thin section samples contain thick layers of large grains (average maximum grain size: 2.5 cm^2) with some being part of the same large-grain layer extending over more than one section, between a depth of 48 and 69 m. Below 62 m grains of similar size are often clustered within sections of heterogeneous size distribution. Almost a third of all sections exhibit a heterogeneous grain size distribution without a clear layered structure. Only one third of all sections have a nearly homogeneous grain size distribution, mostly in the firn and very close to bedrock.

4.3 High-resolution Physical Properties

Following the stratigraphic observations we acknowledge the need to study fabric and microstructure on a smaller-than-section scale. We show the results from the high-resolution centimeter-scale analysis for all measured ice core intervals in Fig. 3. The c-axis eigenvalue λ_3 is given, together with the mean grain size $\bar{A}$, grain and bubble number, and the particle dust record from continuous flow analysis (Bohleber et al., 2018). A depth interval is shown in detail in Fig. 4, including the density ρ and bubble area A_b.

Table 3. Observations from visual stratigraphy line scan images (Fig. B.3). Several zones are identified by changes in the qualitative description; changes in inclination occur in slightly different depth zones. Inclination is counted from the horizontal perpendicular to the ice core axis.

Zone	Depth	Qualitative description	Inclination
I	$0-14\,\mathrm{m}$	bands (thinner than 25 cm) of weak contrast	$0-43\,\mathrm{m}$:
II	$14-38\,\mathrm{m}$	well-defined transitions between lighter/darker bands with decreasing thickness, bands ($<10\,\mathrm{cm}$) disappear at the firn-ice-transition	$5-15°$ in 59 % of images, varying strongly
III	$38-55\,\mathrm{m}$	more uniform appearance, thickness of weakly discernible alternating bands exceeds those of zone II	$43-51\,\mathrm{m}$: no or little inclination
IV	$55-64\,\mathrm{m}$	clearer banding without well-defined transitions	$51-63\,\mathrm{m}$: $10-15°$
V	$64-71\,\mathrm{m}$	layers $\sim$cm with good contrast, but increasingly irregular appearance	$63\,\mathrm{m}$ – bedrock:
VI	$71-72\,\mathrm{m}$	uniform appearance	$15-20°$, max. $30°$

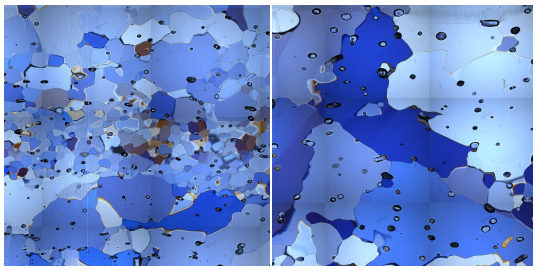

Figure 2. FA image details ($2.5 \times 2.5\,\mathrm{cm}^2$). Left: Example of a fine-grained layer. Right: Example of a coarse-grained layer.

The high-resolution analysis reveals an extreme variability in the fabric and microstructure parameters on the sub-decimeter scale with gradients in eigenvalue of up to 0.2 over a few centimeters. The uncertainty is small compared to the variations. The difference between extreme values within an interval is roughly twice as high as when comparing per-section eigenvalues (Table 2). Below 53 m depth the eigenvalue appears to spike towards lower values while it is high on average (Figure 3), matching the observation of layers with larger and less oriented grains within a more strongly oriented matrix. Fine-grained layers cannot be resolved well as they are often thinner than the sliding computation window. The variability in the c-axis eigenvalue is accompanied by an equally variable mean grain size which is changing often in accordance with the eigenvalue, with a significant (Spearman's) rank correlation coefficient (r_s) of $-0.33 < r_\mathrm{s} < -0.79$ for 8 out of 13 intervals (Appendix C: correlation computation). The anticorrelation between the mean grain size and the number of bubbles N_b is strong in all intervals ($-0.38 < r_\mathrm{s} < -0.91$). In 10 out of 13 intervals we obtain significant correlation coefficients between the mean grain size and the dust content ($-0.51 < r_\mathrm{s} < -0.9$). The close-up from 43 m depth (Fig. 4) shows that for a higher density ρ there are more but smaller bubbles ($0.56 < r_\mathrm{s} < 0.87$ above 44 m depth). Furthermore, the density at this depth changes in accordance with the dust content.

5 Discussion

5.1 Depth-evolution of Crystal Anisotropy

The presented data of crystal-preferred orientation from a non-temperate, midlatitude, high-altitude glacier shows clearly that the development of an anisotropic CPO is not confined to the larger scale of polar ice sheets. In contrast, already in the firn, at one third of the glacier depth, we observe an anisotropic CPO pattern, as has been hypothesized by Diez et al. (2014) following a seismic velocity analysis at the site. The dominant fabric type is a single-maximum, which, in the upper part of the glacier, results from vertical compression in the firn and across the firn-ice transition, and may be enhanced by simple shear due to the surface slope at the flank of CG. In the lower third of the ice core, the inclined single maximum is consistent with simple shear (Azuma, 1994; Llorens et al., 2017; Qi et al., 2019, in press), as we can assume that the glacier is frozen to bedrock. This assessment is further supported by a recent ice-flow model for Colle Gnifetti (Licciulli, 2018), yielding high vertical strain rates $\dot{\varepsilon}_{zz} < 1.9{\cdot}10^{-9}\,\mathrm{s}^{-1}$ and an elevated horizontal strain rate $\dot{\varepsilon}_{zy}$ in the upper 10 m of the firn, and a steadily increasing horizontal strain rate from 30 m depth to bedrock ($\dot{\varepsilon}_{zy} < 2.9 \cdot 10^{-10}\,\mathrm{s}^{-1}$). The faint girdle pattern we see in the Schmidt diagrams of the last 10 m above bedrock is indicative of a component of diverging flow (A. J. Gow & Meese, 2007). This suggests a more complex flow pattern in the bottom part of the glacier than the surface flowline implies at the KCC drilling site (Bohleber et al., 2018). It runs towards the eastern ice cliff, possibly with a component of extensional flow towards the saddle. However, the girdle is not as clearly recognized in single sections of individual intervals, supporting our approach of assessing continuously measured intervals to obtain a better representation of the crystal anisotropy for a given depth. When examined individually, some thin section samples exhibit specific structures, which are, in fact, contributing to the interval girdle. Figure 5a shows steeply inclined bands of crystals with higher colatitude (darker red) that deviate from the surrounding grain matrix. We interpret these to be tilted-lattice bands, which, for polar ice cores, have been shown to indicate small-scale folding (Jansen et al., 2016). In Fig. 5b a number of grains distributed over the section are constituting a second maximum of c-axes which is oriented approximately 90° from the dominant single maximum towards the horizontal. It is currently not resolved why these grains deviate from the matrix but a second maximum is usually interpreted as a consequence of recrystallisation under simple shear conditions (Alley, 1992; Qi et al., 2019, in press).

By including anisotropic deformation and the most relevant recrystallisation mechanisms in a microstructural model, Llorens et al. (2016) find that the grain size is mainly controlled by the recrystallisation processes, accompanied by secondary effects like grain dissection (Steinbach et al., 2017). Thus, the observed grain size variability with concentrations of very large or small grains is indicative of ongoing recrystallisation in this shallow mountain glacier. Exemplary microstructure images are shown in appendix B, Fig. B.2, illustrating the occurrence of various grain and subgrain topological features such as bulging GBs and intricate subgrain boundary structures. These are typically observed in polar firn and ice as well as experimentally deformed ice under comparably low stress undergoing dynamic recrystallisation (Hamann, Weikusat, Azuma, & Kipfstuhl, 2007; Kipfstuhl et al., 2009; Weikusat, Kuiper, Pennock, Kipfstuhl, & Drury, 2017), but the discussion of further microstructural parameters is beyond the intended scope of this paper.

5.2 Short-scale Variability

Our analyses on the sub-section scale show that layers of distinct grain size and layers of varying fabric strength can be observed at many depths. The variations are much stronger than previously known from low-resolution studies which could imply effects on the integrity of stratigraphic records (Faria et al., 2010) and also be highly relevant for the interpretation of geophysical data to map intraglacial structures (Diez et al., 2015; Eisen et al., 2007; Fujita, Maeno, & Matsuoka, 2006; Hofstede, Diez, Eisen, Jansen, &

Kristoffersen, 2012; Horgan et al., 2008; Kerch, Diez, Weikusat, & Eisen, 2018; Matsuoka et al., 2003). The comparison of high-resolution data series reveals a good correlation between the presented microstructural parameters, but it is very difficult to establish the order of causal dependencies; feedbacks between coupled processes are very probable.

There is evidence on a large spatio-temporal scale in ice cores, that the microstructure could be governed by the impurity content (Durand, Weiss, et al., 2006). However, the process identified to be the main driver for this relation (Zener pinning) is under discussion (Eichler et al., 2017). This raises the question whether the same mechanisms could also play a role on the cm-scale? Our results strongly suggest that this is the case as particle content and mean grain size show a strong anticorrelation. While the ice from Colle Gnifetti is relatively pure for a midlatitude glacier due to the high altitude, its dust content exceeds the dust load in Holocene ice from polar cores by a factor of 10 (Wagenbach & Geis, 1989), increasing the chance of observing a connection between microstructure and particle content. Recently developed techniques such as LA-ICP-MS (Della Lunga, Müller, Rasmussen, Svensson, & Vallelonga, 2017; Reinhardt et al., 2001; Spaulding et al., 2017) could provide spatially resolved data on particle distribution with respect to microstructural features to study the interaction processes in detail.

Another parameter which is highly variable from the deposition processes on the glacier surface is the density. Extremes in density are melt layers that are observed not only in alpine glaciers but also in polar ice sheets (Schaller et al., 2016). We cannot directly connect outstanding layers in microstructure or fabric with original melt layers. However, even without melt layers, initial density fluctuations in the snow, which could be linked to the concentration of calcium in polar cores (Hrhold et al., 2012), can be expected to evolve into a sequence of layers in which bubbles have different characteristics, e.g. many small bubbles or fewer large bubbles. Steinbach et al. (2016) show in their microstructure model how bubbles can initiate strain localisation. In our data we see a clear connection between the bubble number density and the mean grain size, which feeds back into the idea that grain size variations are connected to density variations (Roessiger, Bons, & Faria, 2014). As mentioned before, Llorens et al. (2016) show that recrystallisation processes are most evident in grain evolution. An existing grain size variability would be enhanced by this.

But how does all this affect the fabric evolution and what are the consequences for the bulk deformation? The small-scale variability in the CPO mostly correlates weakly with the microstructure variability in general, with local exceptions of strong correlation, especially where there is a strong contrast in microstructure parameters. Thus, the role of the microstructure variations for the fabric variations appears to be that of initial perturbations which subsequently lead to local enhancement of strain rate. This has been hypothesized before (Montagnat et al., 2014) but has not been presented with much evidence due to a lack of continuous data. As a result of locally enhanced deformation small-scale shear zones (Hudleston, 2015) might develop. This would, in turn, allow for thick layers of ice deforming at a lower rate to be dominated by recrystallisation. However, we do not have information on the lateral scale to draw conclusions on the effect on the bulk deformation. We certainly recommend to collect high-resolution borehole deformation data to be able to connect fabric information and in-situ deformation on this particular length scale, e.g. by means of ultrasonic profiling (Gusmeroli, Pettit, Kennedy, & Ritz, 2012), even if they can only provide a reduced two-dimensional representation of CPO. Our results are in line with Svensson, Baadsager, Persson, Hvidberg, and Siggaard-Andersen (2003) who conducted a case study on the seasonal variability in ice crystal properties on the cm-scale and observe small-grain layers corresponding to the spring season but cannot find a seasonal variability of the c-axis orientations. Additionally, we find no evidence of a connection between the thickness of fabric layers with the thickness of annual layers as determined from impurity records (Bohleber et al., 2018).

5.3 Do We Need a New Scale-sensitive Statistical Approach?

From a methodological standpoint, our study provides evidence that, a priori, one thin section sample does not provide sufficient statistics to draw reliable conclusions for a depth interval of several tens of meters. An apparent fabric variability may simply be the result of statistical undersampling. The statistical uncertainty as proposed by Durand, Gagliardini, et al. (2006) does not appear to be an appropriate uncertainty measure for our data if this uncertainty is supposed to account for the variation in adjacent samples. Consequently, the task at hand is to establish which sample length scale is in fact representative for a given interval-of-interest. The same holds for the sampling interval, i.e. the distance between samples where no measurements are conducted. This sampling interval and the sample length make it mandatory to readdress the estimation of an appropriate statistical error based on such representative scales.

Furthermore, our results demonstrate that the choice of a representative length scale for CPO data is also dependent on the research question, considering the activity of several contributing and coupled processes on different length scales. More specific, the evaluation of fabric data needs to be adjusted to the resolution of complementary methods applied to the ice core or glacier, e.g. radar and seismics as well as continuous logging techniques, to advance our understanding of glaciological processes across different methodological approaches and spatial scales.

6 Conclusions

This study confirms the observation of a comparable development of crystal anisotropy in cold alpine glaciers and in polar glaciers or ice sheets, despite a factor of 35 (compared with the NEEM ice core) difference in thickness. Additionally, we observe and describe a strong variability in the microstructural parameters and crystal orientation during a high-resolution analysis of continuous measurement intervals. Thus, we can assume that this variability should also develop in polar glaciers, which emphasizes the usefulness of non-polar glacier environments for the study of glacial processes in general. We consider different causes for the variability, recognising that different causes may dominate on different length scales. Acknowledging the interconnectivity of the analysed parameters, we conclude that the high variability in CPO may develop as a result of deformation localisation (shear zones) on different length scales, following initial differences in density and microstructural parameters which, in turn, are influenced by the impurity concentration and the seasonal cycle of environmental conditions. The possible consequences of such shear zones on bulk deformation (e.g. folds) and the interpretation of stratigraphic parameters are still under investigation (Bons et al., 2016; Montagnat et al., 2013; Ran et al., 2018).

Our results lead us to question the current single-section mode of CPO evaluation and call for a new statistical approach based on a higher and scale-specific data coverage, and/or an adjusted uncertainty estimate. Furthermore, our findings reinforce the demand for high-resolution and high-coverage proxy methods (e.g. ultrasonic sounding in the borehole and the laboratory (Mikesell, van Wijk, Otheim, Marshall, & Kurbatov, 2017; Vaughan, van Wijk, Prior, & Bowman, 2016), high-resolution dielectric profiling (Wilhelms, 2005), polarimetric radar (Drews et al., 2012; J. Li et al., 2018) and seismics (Kerch, Diez, et al., 2018)) to be applied in order to obtain a more complete understanding of the vertical and lateral crystal anisotropy structure and its role for large-scale glacier deformation.

Table A.1. Resolution of fabric studies on polar ice cores. *Section* refers to a typically 10 cm long thin section sample; *continuous* refers to measurements of several adjacent sections in an ice core segment or bag.

Authors	Ice core	Length [m]	Fabric resolution; intervals between samples	estimated % of total length
A. Gow et al. (1997)	GISP2	3054	ca. 500 sections	1.7 %
Thorsteinsson, Kipfstuhl, and Miller (1997)	GRIP	3029	ca. 100 sections; mostly 25–55 m intervals	0.3 %
Wang et al. (2002)	NGRIP	2930	142 sections; 5–66 m intervals	0.5 %
Montagnat et al. (2014), Eichler, Weikusat, and Kipfstuhl (2013)	NEEM	2540	ca. 700 sections; 10 m intervals, partially continuous (bags of 55 cm)	3 %
Treverrow, Jun, and Jacka (2016)	Dome Summit South	1196	185 sections; 5–6 m intervals	0.9 %
Azuma et al. (1999)	Dome Fuji	2500	ca. 240 sections; 20 m interval, partially continuous	1 %
A. J. Gow and Meese (2007), DiPrinzio et al. (2005)	Siple Dome	1004	ca. 100 sections; 20 m intervals	1 %
Wang, Kipfstuhl, Azuma, Thorsteinsson, and Miller (2003), Durand et al. (2007, 2009)	EPICA Dome C	3260	ca. 200 sections; 11–50 m intervals	0.7 %
Weikusat, Jansen, et al. (2017)	EPICA DML	2774	210 sections; 50 m intervals, partially continuous	0.8 %
Montagnat et al. (2012)	Talos Dome	1620	10–20 m intervals	1 %
Fitzpatrick et al. (2014)	WAIS	3405	20 m intervals	0.5 %

A Collection of major polar fabric studies from the last 20 years

B Complementary figures

C Correlation computation for cm-scale data series

As the data are in general not normally distributed we compute correlation coefficients between various data sets available in this study by considering the ranks of the bivariate data (Spearman correlation coefficient)

$$r_\mathrm{s} = 1 - \frac{6 \sum_{i=1}^{n} d_i^2}{n(n^2-1)} \tag{C.1}$$

with the sample size of paired values n, the rank difference d and $-1 < r_\mathrm{s} < 1$. The significance of the obtained correlation coefficient is tested. The data of this study can be regarded as a time series for which each data point is not necessarily independent of

its neighbours (Mudelsee, 2003, "serial dependence"). The autocorrelation of a data series of length n for a lag τ is used to evaluate the non-randomness of the data and provide the distance or time lag within which subsequent data points cannot be considered as independent. Considering τ and the short length of data sequences computed from continuous fabric data we derive an effective sample size, i.e. smaller than the original sample size, from which a correlation with another data set might be calculated under the assumption of randomness of the data points. Only eigenvalues calculated from successive, but not overlapping, frames are used to derive correlation coefficients, which limits the sample size to 50 data points per meter. By choosing a different frame set that is shifted by $2n$ mm (with n = [1,9]) and repeated calculation we obtain several values for the correlation coefficient for the same continuous interval, providing a robust estimate of correlation on the 2 cm scale. All bivariate data sets are downsampled to the lower resolution of the two variables.

Acknowledgments

The data sets for the ice core KCC (fabric, microstructure, eigenvalues, density, linescans) are published in the open-access database PANGAEA®(Kerch, Eisen, et al., 2018, doi:10.1594/PANGAEA.887838) and also available upon request.

We would like to thank the KCC drilling and processing team with collegues from the Institute of Environmental Physics, Heidelberg University, Germany (Helene Hoffmann, Martin Hackel), the Climate Change Institute, University of Maine, USA (Nicole Spaulding) and the Institute for Climate and Environmental Physics, University of Bern, Switzerland (Remo Walther, Samuel Marending, Jakob Schwander, Tobias Erhardt). We thank Hubertus Fischer for providing the dedicated drill equipment and the support with CFA measurements done in his laboratories in Bern. We are grateful for the support from members of the AWI glaciology and the junior group "Deformation mechanisms" in the ice laboratory and for many fruitful discussions, especially Sepp Kipfstuhl, Daniela Jansen, Florian Steinbach and Ernst-Jan Kuiper. J.K. was funded by a scholarship of the Studienstiftung des deutschen Volkes and supported by the work group *Klimaarchiv Eis* lead by Dietmar Wagenbach, and HGF grant no. VH-NG-803 to I.W.; O.E. and J.K. were partly supported by the DFG Emmy Noether programme grant EI 672/5-1. We dedicate this paper to the memory of Dietmar Wagenbach.

References

Adam, J. F. (1989). Methoden und algorithmen zur verwaltung und analyse axialer 3-d-richtungsdaten und ihrer belegungsdichten. *Goettinger Arb. Geol. Palaontol.*, *40*, 100.

Alean, J., Haeberli, W., & Schdler, B. (1983). Snow accumulation, firn temperature and solar radiation in the area of the colle gnifetti core drilling site (monte rosa, swiss alps): distribution patterns and interrelationships. *Z. Gletscherkd. Glazialgeol.*, *19*(2), 131–147.

Allen, C., Kamb, W., Meier, M., & Sharp, R. (1960). Structure of the lower blue glacier, washington. *Journal of Geology*, 601–625.

Alley, R. B. (1992). Flow-law hypotheses for ice-sheet modeling. *J. Glaciol.*, *38*(129), 245–256.

Anderson, M., Grest, G., & Srolovitz, D. (1989). Computer simulation of normal grain growth in three dimensions. *Philos. Mag. B*, *59*(3), 293–329.

Azuma, N. (1994). A flow law for anisotropic ice and its application to ice sheets. *Earth Planet. Sci. Lett.*, *128*, 601–614. doi: 10.1016/0012-821X(94)90173-2

Azuma, N., & Goto-Azuma, K. (1996). An anisotropic flow law for ice-sheet ice and its implications. *Ann. Glaciol.*, *23*, 202–208.

Azuma, N., & Higashi, A. (1985). Formation processes of ice fabric pattern in ice sheets. *Ann. Glaciol.*, *6*, 130–134.

Azuma, N., Miyakoshi, T., Yokoyama, S., & Takata, M. (2012). Impeding effect of air bubbles on normal grain growth of ice. *J. Struct. Geol.*, *42*, 184–193. doi: 10.1016/j.jsg.2012.05.005

Azuma, N., Wang, Y., Mori, K., Narita, H., Hondoh, T., Shoji, H., & Watanabe, O. (1999). Textures and fabrics in the dome f (antarctica) ice core. *Ann. Glaciol.*, *29*(1), 163–168. doi: 10.3189/172756499781821148

Binder, T., Garbe, C., Wagenbach, D., Kipfstuhl, S., & Freitag, J. (2013). Extraction and parametrization of grain boundary networks in glacier ice, using a dedicated method of automatic image analysis. *J. Microsc.*, *250*, 130–141. doi: 10.1111/jmi.12029

Bohleber, P., Erhardt, T., Spaulding, N., Hoffmann, H., Fischer, H., & Mayewski, P. (2018). Temperature and mineral dust variability recorded in two low-accumulation alpine ice cores over the last millennium. *Clim. Past*, *14*(1), 21–37. doi: 10.5194/cp-14-21-2018

Bohleber, P., Wagenbach, D., Schner, W., & Bhm, R. (2013). To what extent do water isotope records from low accumulation alpine ice cores reproduce instrumental temperature series? *Tellus B*, *65*, 1–17. doi: 10.3402/tellusb.v65i0.20148

Bons, P. D., Jansen, D., Mundel, F., Bauer, C. C., Binder, T., Eisen, O., ... Weikusat, I. (2016). Converging flow and anisotropy cause large-scale folding in greenland's ice sheet. *Nat. Commun.*, *7*, 11427. doi: 10.1038/ncomms11427

Della Lunga, D., Müller, W., Rasmussen, S. O., Svensson, A., & Vallelonga, P. (2017). Calibrated cryo-cell uv-la-icpms elemental concentrations from the ngrip ice core reveal abrupt, sub-annual variability in dust across the gi-21.2 interstadial period. *The Cryosphere*, *11*(3), 1297–1309. doi: 10.5194/tc-11-1297-2017

Diez, A., Eisen, O., Hofstede, C., Lambrecht, A., Mayer, C., Miller, H., ... Weikusat, I. (2015). Seismic wave propagation in anisotropic ice part 2: Effects of crystal anisotropy in geophysical data. *The Cryosphere*, *9*, 385–398. doi: 10.5194/tc-9-385-2015

Diez, A., Eisen, O., Weikusat, I., Eichler, J., Hofstede, C., Bohleber, P., ... Polom, U. (2014). Influence of ice crystal anisotropy on seismic velocity analysis. *Ann. Glaciol.*, *55*(67), 97–106. doi: 10.3189/2014AoG67A002

DiPrinzio, C. L., Wilen, L. A., Alley, R., Fitzpatrick, J., Spencer, M., & Gow, A. (2005). Fabric and texture at siple dome, antarctica. *J. Glaciol.*, *51*(173), 281–290. doi: 10.3189/172756505781829359

Drews, R., Eisen, O., Steinhage, D., Weikusat, I., Kipfstuhl, S., & Wilhelms, F. (2012). Potential mechanisms for anisotropy in ice-penetrating radar data. *J. Glaciol.*, *58*(209), 613–624. doi: 10.3189/2012JoG11J114

Durand, G., Gagliardini, O., Thorsteinsson, T., Svensson, A., Kipfstuhl, S., & Dahl-Jensen, D. (2006). Ice microstructure and fabric: an up-to-date approach for measuring textures. *J. Glaciol.*, *52*(179), 619–630. doi: 10.3189/172756506781828377

Durand, G., Gillet-Chaulet, F., Svensson, A., Gagliardini, O., Kipfstuhl, S., Meyssonnier, J., ... Dahl-Jensen, D. (2007). Change in ice rheology during climate variations implications for ice flow modelling and dating of the epica dome c core. *Clim. Past*, *3*, 155–167.

Durand, G., Svensson, A., Persson, A., Gagliardini, O., Gillet-Chaulet, F., Sjolte, J., ... Dahl-Jensen, D. (2009). Evolution of the texture along the epica dome c ice core. *Low Temperature Science*, *68*, 91–105.

Durand, G., Weiss, J., Lipenkov, V., Barnola, J. M., Krinner, G., Parrenin, F., ... Bigler, M. (2006). Effect of impurities on grain growth in cold ice sheets. *J. Geophys. Res.*, *111*, 1–18. doi: 10.1029/2005JF000320

Duval, P., Ashby, M., & Anderman, I. (1983). Rate-controlling processes in the

creep of polycrystalline ice. *J. Phys. Chem.*, *87*(21), 4066–4074. doi: 10.1021/j100244a014

Eichler, J. (2013). *C-axis analysis of the neem ice core – an approach based on digital image processing* (Diploma thesis, Freie Universität Berlin and Alfred-Wegener-Institut Bremerhaven). Retrieved from `epic.awi.de/33070/`

Eichler, J., Kleitz, I., Bayer-Giraldi, M., Jansen, D., Kipfstuhl, S., Shigeyama, W., ... Weikusat, I. (2017). Location and distribution of micro-inclusions in the edml and neem ice cores using optical microscopy and in situ raman spectroscopy. *The Cryosphere*, *11*(3), 1075–1090. doi: 10.5194/tc-11-1075-2017

Eichler, J., Weikusat, I., & Kipfstuhl, S. (2013). *C-axis fabric analysis of ice samples collected from the neem ice core* [data set]. PANGAEA. doi: 10.1594/PANGAEA.838063

Eisen, O., Hamann, I., Kipfstuhl, S., Steinhage, D., & Wilhelms, F. (2007). Direct evidence for continuous radar reflector originating from changes in crystal-orientation fabric. *The Cryosphere*, *1*, 1–10. doi: 10.5194/tc-1-1-2007

Faria, S. H., Freitag, J., & Kipfstuhl, S. (2010). Polar ice structure and the integrity of ice-core paleoclimate records. *Quat. Sci. Rev.*, *29*(1), 338–351. doi: 10.1016/j.quascirev.2009.10.016

Faria, S. H., Weikusat, I., & Azuma, N. (2014a). The microstructure of polar ice. part i: Highlights from ice core research. *J. Struct. Geol.*, *61*, 2–20. (Microdynamics of Ice) doi: 10.1016/j.jsg.2013.09.010

Faria, S. H., Weikusat, I., & Azuma, N. (2014b). The microstructure of polar ice. part ii: State of the art. *J. Struct. Geol.*, *61*, 21–49. (Microdynamics of Ice) doi: 10.1016/j.jsg.2013.11.003

Fitzpatrick, J. J., Voigt, D. E., Fegyveresi, J. M., Stevens, N. T., Spencer, M. K., Cole-Dai, J., ... McConnell, J. R. (2014). Physical properties of the wais divide ice core. *J. Glaciol.*, *60*(224), 1181–1198. doi: 10.3189/2014JoG14J100

Freitag, J., Wilhelms, F., & Kipfstuhl, S. (2004). Microstructure-dependent densification of polar firn derived from x-ray microtomography. *J. Glaciol.*, *50*(169), 243–250. doi: 10.3189/172756504781830123

Fujita, S., Maeno, H., & Matsuoka, K. (2006). Radio-wave depolarization and scattering within ice sheets: a matrix-based model to link radar and ice-core measurements and its application. *J. Glaciol.*, *52*(178), 407–424. doi: 10.3189/172756506781828548

Gagliardini, O., Durand, G., & Wang, Y. (2004). Grain area as a statistical weight for polycrystal constituents. *J. Glaciol.*, *50*(168), 87–95. doi: 10.3189/172756504781830349

Gerbi, C. C., Mills, S. G., Bernsen, S., Lee, I. R., Clemens-Sewall, D., Hruby, K., ... Kreutz, K. J. (2018). Crystallographic orientations in the lateral margin of jarvis glacier, eastern alaska range..

Gow, A., Meese, D., Alley, R., Fitzpatrick, J., Anandakrishnan, S., Woods, G., & Elder, B. (1997). Physical and structural properties of the greenland ice sheet project 2 ice core: A review. *J. Geophys. Res.*, *102*(C12), 26559–26575. doi: 10.1029/97JC00165

Gow, A. J., & Meese, D. A. (2007). Physical properties, crystalline textures and c-axis fabrics of the siple dome (antarctica) ice core. *J. Glaciol.*, *53*(183), 573–584. doi: 10.3189/002214307784409252

Graham, F. S., Morlighem, M., Warner, R. C., & Treverrow, A. (2018). Implementing an empirical scalar constitutive relation for ice with flow-induced polycrystalline anisotropy in large-scale ice sheet models. *The Cryosphere*, *12*(3), 1047–1067. doi: 10.5194/tc-12-1047-2018

Gusmeroli, A., Pettit, E. C., Kennedy, J. H., & Ritz, C. (2012). The crystal fabric of ice from full-waveform borehole sonic logging. *J. Geophys. Res.*, *117*, 1–13. doi: 10.1029/2012JF002343

Hamann, I., Weikusat, C., Azuma, N., & Kipfstuhl, S. (2007, May). Evolution of

ice crystal microstructures during creep experiments. *J. Glaciol.*, *53*(182), 479-489. doi: 10.3189/002214307783258341

Heilbronner, R., & Barrett, S. (2014). *Image analysis in earth sciences: Microstructures and textures of earth materials*. Springer.

Hellmann, S., Kerch, J., Bauder, A., & Maurer, H. (2018). Crystal orientation fabric analysis on ice core samples from a temperate alpine glacier..

Higashi, A. (1967). Ice crystal growth in a temperate glacier in alaska. *Physics of Snow and Ice: Proceedings*, *1*(1), 409–430.

Hoelzle, M., Darms, G., Lthi, M., & Suter, S. (2011). Evidence of accelerated englacial warming in the monte rosa area, switzerland/italy. *The Cryosphere*, *5*(1), 231–243. doi: 10.5194/tc-5-231-2011

Hoffmann, H., Preunkert, S., Legrand, M., Leinfelder, D., Bohleber, P., Friedrich, R., & Wagenbach, D. (2017). A new sample preparation system for micro-14 c dating of glacier ice with a first application to a high alpine ice core from colle gnifetti (switzerland). *Radiocarbon*, 1–17. doi: 10.1017/RDC.2017.99

Hofstede, C., Diez, A., Eisen, O., Jansen, D., & Kristoffersen, Y. (2012). A combined vibroseis-explosive survey at halvfarryggen, a local ice dome in east antarctica.. Retrieved from `http://epic.awi.de/31890/`

Hooke, R. L. (1973). Structure and flow in the margin of the barnes ice cap, baffin island, nwt, canada. *J. Glaciol.*, *12*(66), 423–438. doi: 10.3198/1973JoG12-66-423-438

Horgan, H. J., Anandakrishnan, S., Alley, R. B., Peters, L. E., Tsoflias, G. P., Voigt, D. E., ... Winberry, J. P. (2008). Complex fabric development revealed by englacial seismic reflectivity: Jakobshavn isbr, greenland. *Geophys. Res. Lett.*, *35*, 1–6. doi: 10.1029/2008GL033712

Hudleston, P. J. (1980). The progressive development of inhomogeneous shear and crystallographic fabric in glacial ice. *J. Struct. Geol.*, *2*(1-2), 189–196. doi: 10.1016/0191-8141(80)90049-8

Hudleston, P. J. (2015). Structures and fabrics in glacial ice: A review. *J. Struct. Geol.*, *81*, 1–27. doi: 10.1016/j.jsg.2015.09.003

Hrhold, M., Laepple, T., Freitag, J., Bigler, M., Fischer, H., & Kipfstuhl, S. (2012). On the impact of impurities on the densification of polar firn. *Earth Planet. Sci. Lett.*, *325–326*, 93–99. doi: 10.1016/j.epsl.2011.12.022

Jansen, D., Llorens Verde, M. G., Westhoff, J., Steinbach, F., Kipfstuhl, S., Bons, P. D., ... Weikusat, I. (2016). Small-scale disturbances in the stratigraphy of the neem ice core: observations and numerical model simulations. *The Cryosphere*, *10*, 359–370. doi: 10.5194/tc-10-359-2016

Jonsson, S. (1970). Structural studies of subpolar glacier ice. *Geografiska Annaler: Series A, Physical Geography*, *52*(2), 129–145. doi: 10.2307/520606

Kamb, W. B. (1959). Ice petrofabric observations from blue glacier, washington, in relation to theory and experiment. *J. Geophys. Res.*, *64*(11), 1891–1909. doi: 10.1029/JZ064i011p01891

Kennedy, J. H., Pettit, E. C., & DiPrinzio, C. L. (2013). The evolution of crystal fabric in ice sheets and its link to climate history. *J. Glaciol.*, *59*(214), 357–373. doi: 10.3189/2013JoG12J159

Kerch, J. (2016). *Crystal-orientation fabric variations on the cm-scale in cold alpine ice: Interaction with paleo-climate proxies under deformation and implications for the interpretation of seismic velocities* (Doctoral dissertation, Ruprecht-Karls-Universität Heidelberg). doi: 10.11588/heidok.00022326

Kerch, J., Diez, A., Weikusat, I., & Eisen, O. (2018). Deriving seismic velocities on the micro-scale from c-axis orientations in ice cores. *The Cryosphere Discuss.*, 1–27. doi: 10.5194/tc-2017-281

Kerch, J., Eisen, O., Eichler, J., Binder, T., Bohleber, P., Freitag, J., ... Weikusat, I. (2018).
doi: 10.1594/PANGAEA.887838

Kipfstuhl, S., Faria, S. H., Azuma, N., Freitag, J., Hamann, I., Kaufmann, P., ... Wilhelms, F. (2009). Evidence of dynamic recrystallization in polar firn. *J. Geophys. Res.*, *114*, 1–10. doi: 10.1029/2008JB005583

Kipfstuhl, S., Hamann, I., Lambrecht, A., Freitag, J., Faria, S. H., Grigoriev, D., & Azuma, N. (2006). Microstructure mapping: a new method for imaging deformation-induced microstructural features of ice on the grain scale. *J. Glaciol.*, *52*(178), 398–406. doi: 10.3189/172756506781828647

Li, J., Vélez González, J. A., Leuschen, C., Harish, A., Gogineni, P., Montagnat, M., ... Paden, J. (2018). Multi-channel and multi-polarization radar measurements around the neem site. *The Cryosphere*, *12*(8), 2689–2705. doi: 10.5194/tc-12-2689-2018

Li, Y., Kipfstuhl, S., & Huang, M. (2017). Ice microstructure and fabric of guliya ice cap in tibetan plateau, and comparisons with vostok3g-1, epica dml, and north grip. *Crystals*, *7*(4). doi: 10.3390/cryst7040097

Licciulli, C. (2018). *Full stokes ice-flow modeling of the high-alpine glacier saddle colle gnifetti, monte rosa: Flow field characterization for an improved interpretation of the ice-core records* (Doctoral dissertation, Ruprecht-Karls-Universität Heidelberg). doi: 10.11588/heidok.00023981

Llorens, M.-G., Griera, A., Bons, P. D., Lebensohn, R. A., Evans, L. A., Jansen, D., & Weikusat, I. (2016). Full-field predictions of ice dynamic recrystallisation under simple shear conditions. *Earth Planet. Sci. Lett.*, *450*, 233 – 242. doi: 10.1016/j.epsl.2016.06.045

Llorens, M.-G., Griera, A., Steinbach, F., Bons, P. D., Gomez-Rivas, E., Jansen, D., ... Weikusat, I. (2017). Dynamic recrystallization during deformation of polycrystalline ice: insights from numerical simulations. *Philos. Trans. R. Soc. London, Ser. A*, *375*(2086). doi: 10.1098/rsta.2015.0346

Martin, C., Gudmundsson, G., Pritchard, H., & Gagliardini, O. (2009). On the effects of anisotropic rheology on ice flow, internal structure, and the age-depth relationship at ice divides. *J. Geophys. Res.*, *114*, 1–18. doi: 10.1029/2008JF001204

Matsuoka, K., Furukawa, T., Fujita, S., Maeno, H., Uratsuka, S., Naruse, R., & Watanabe, O. (2003). Crystal orientation fabrics within the antarctic ice sheet revealed by a multipolarization plane and dual-frequency radar survey. *J. Geophys. Res.*, *108*(B10). doi: 10.1029/2003JB002425

Meier, M. F., Rigsby, G. P., & Sharp, R. P. (1954). Preliminary data from saskatchewan glacier, alberta, canada. *Arctic*, *7*(1), 3–26.

Mikesell, T. D., van Wijk, K., Otheim, L. T., Marshall, H.-P., & Kurbatov, A. (2017). Laser ultrasound observations of mechanical property variations in ice cores. *Geosciences*, *7*(3). doi: 10.3390/geosciences7030047

Montagnat, M., Azuma, N., Dahl-Jensen, D., Eichler, J., Fujita, S., Gillet-Chaulet, F., ... Weikusat, I. (2014). Fabric along the neem ice core, greenland, and its comparison with grip and ngrip ice cores. *The Cryosphere*, *8*(4), 1129–1138. doi: 10.5194/tc-8-1129-2014

Montagnat, M., Buiron, D., Arnaud, L., Broquet, A., Schlitz, R., Jacob, R., & Kipfstuhl, S. (2012). Measurements and numerical simulation of fabric evolution along the talos dome ice core, antarctica. *Earth Planet. Sci. Lett.*, *357*, 168–178. doi: 10.1016/j.epsl.2012.09.025

Montagnat, M., Castelnau, O., Bons, P., Faria, S., Gagliardini, O., Gillet-Chaulet, F., ... Suquet, P. (2013). Multiscale modeling of ice deformation behavior. *J. Struct. Geol.*, *61*, 78–108. doi: 10.1016/j.jsg.2013.05.002

Monz, M., & Hudleston, P. (2018). Microfabric and structures in glacial ice: A case study of storglaciären, sweden. In *Egu general assembly conference abstracts* (Vol. 20, p. 10077).

Mudelsee, M. (2003). Estimating pearson's correlation coefficient with bootstrap confidence interval from serially dependent time series. *Mathematical Geology*,

35(6), 651–665. doi: 10.1023/B:MATG.0000002982.52104.02

Peternell, M., Kohlmann, F., Wilson, C. J. L., Seiler, C., & Gleadow, A. J. W. (2009). A new approach to crystallographic orientation measurement for apatite fission track analysis: Effects of crystal morphology and implications for automation. *Chem. Geol.*, *265*, 527–539. doi: 10.1016/j.chemgeo.2009.05.021

Pettit, E. C., Thorsteinsson, T., Jacobson, H. P., & Waddington, E. D. (2007). The role of crystal fabric in flow near an ice divide. *J. Glaciol.*, *53*(181), 277–288. doi: 10.3189/172756507782202766

Preunkert, S., Wagenbach, D., Legrand, M., & Vincent, C. (2000). Col du dôme (mt blanc massif, french alps) suitability for ice-core studies in relation with past atmospheric chemistry over europe. *Tellus B: Chemical and Physical Meteorology*, *52*(3), 993–1012. doi: 10.3402/tellusb.v52i3.17081

Qi, C., Prior, D. J., Craw, L., Fan, S., Llorens, M.-G., Griera, A., ... Goldsby, D. L. (2019, in press). Crystallographic preferred orientations of ice deformed in direct-shear experiments at low temperatures. *The Cryosphere*, *2018*, 1–35. doi: 10.5194/tc-2018-140

Ran, H., de Riese, T., Llorens, M.-G., Finch, M. A., Evans, L. A., Gomez-Rivas, E., ... Bons, P. D. (2018). Time for anisotropy: The significance of mechanical anisotropy for the development of deformation structures. *J. Struct. Geol.*. doi: 10.1016/j.jsg.2018.04.019

Reinhardt, H., Kriews, M., Miller, H., Schrems, O., Lüdke, C., Hoffmann, E., & Skole, J. (2001). Laser ablation inductively coupled plasma mass spectrometry: a new tool for trace element analysis in ice cores. *Fresenius J. Anal. Chem.*, *370*(5), 629–636. doi: 10.1007/s002160100853

Rigsby, G. P. (1951). Crystal fabric studies on emmons glacier mount rainier, washington. *The Journal of Geology*, *59*(6), 590–598.

Rigsby, G. P. (1960). Crystal orientation in glacier and in experimentally deformed ice. *J. Glaciol.*, *3*(27), 589–606.

Roessiger, J., Bons, P. D., & Faria, S. H. (2014). Influence of bubbles on grain growth in ice. *J. Struct. Geol.*, *61*, 123–132. doi: 10.1016/j.jsg.2012.11.003

Schaller, C. F., Freitag, J., Kipfstuhl, S., Laepple, T., Steen-Larsen, H. C., & Eisen, O. (2016). A representative density profile of the north greenland snowpack. *The Cryosphere*, *10*(5), 1991–2002. doi: 10.5194/tc-10-1991-2016

Schulson, E. M., & Duval, P. (2009). *Creep and fracture of ice.* Cambridge University Press.

Schwikowski, M., Brütsch, S., Gäggeler, H., & Schotterer, U. (1999). A high-resolution air chemistry record from an alpine ice core: Fiescherhorn glacier, swiss alps. *J. Geophys. Res.*, *104*(D11), 13709–13719. doi: 10.1029/1998JD100112

Seddik, H., Greve, R., Placidi, L., Hamann, I., & Gagliardini, O. (2008). Application of a continuum-mechanical model for the flow of anisotropic polar ice to the edml core, antarctica. *J. Glaciol.*, *54*(187), 631–642. doi: 10.3189/002214308786570755

Spaulding, N. E., Sneed, S. B., Handley, M. J., Bohleber, P., Kurbatov, A. V., Pearce, N. J., ... Mayewski, P. A. (2017). A new multielement method for la-icp-ms data acquisition from glacier ice cores. *Environ. Sci. Technol.*, *51*(22), 13282–13287. doi: 10.1021/acs.est.7b03950

Steinbach, F., Bons, P. D., Griera, A., Jansen, D., Llorens, M.-G., Roessiger, J., & Weikusat, I. (2016). Strain localization and dynamic recrystallization in the ice–air aggregate: a numerical study. *The Cryosphere*, *10*(6), 3071–3089. doi: 10.5194/tc-10-3071-2016

Steinbach, F., Kuiper, E.-J. N., Eichler, J., Bons, P. D., Drury, M. R., Griera, A., ... Weikusat, I. (2017). The relevance of grain dissection for grain size reduction in polar ice: insights from numerical models and ice core microstructure analysis. *Frontiers in Earth Science*, *5*, 66. doi: 10.3389/feart.2017.00066

Svensson, A., Baadsager, P., Persson, A., Hvidberg, C. S., & Siggaard-Andersen, M.-L. (2003). Seasonal variability in ice crystal properties at northgrip: a case study around 301 m depth. *Ann. Glaciol.*, *37*(1), 119–122.

Svensson, A., Nielsen, S. W., Kipfstuhl, S., Johnsen, S. J., Steffensen, J. P., Bigler, M., ... Rthlisberger, R. (2005). Visual stratigraphy of the north greenland ice core project (northgrip) ice core during the last glacial period. *J. Geophys. Res.*, *110*(D2). doi: 10.1029/2004JD005134

Taylor, L. D. (1963). Structure and fabric on the burroughs glacier, south-east alaska. *J. Glaciol.*, *4*(36), 731–752. doi: 10.3189/S0022143000028331

Thompson, L. G., Mosley-Thompson, E., Brecher, H., Davis, M., León, B., Les, D., ... Mountain, K. (2006). Abrupt tropical climate change: Past and present. *PNAS*, *103*(28), 10536–10543. doi: 10.1073/pnas.0603900103

Thompson, L. G., Mosley-Thompson, E., Davis, M., Lin, P., Dai, J., Bolzan, J., & Yao, T. (1995). A 1000 year climate ice-core record from the guliya ice cap, china: its relationship to global climate variability. *Ann. Glaciol.*, *21*, 175–181. doi: 10.3189/S0260305500015780

Thorsteinsson, T., Kipfstuhl, J., & Miller, H. (1997). Textures and fabrics in the grip ice core. *J. Geophys. Res.*, *102*(C12), 26583–26599. doi: 10.1029/97JC00161

Tison, J.-L., & Hubbard, B. (2000). Ice crystallographic evolution at a temperate glacier: Glacier de tsanfleuron, switzerland. *Geological Society, London, Special Publications*, *176*, 23–38. doi: 10.1144/GSL.SP.2000.176.01.03

Treverrow, A., Jun, L., & Jacka, T. H. (2016). Ice crystal c-axis orientation and mean grain size measurements from the dome summit south ice core, law dome, east antarctica. *Earth Syst. Sci. Data*, *8*(1), 253–263. doi: 10.5194/essd-8-253-2016

Vallon, M., Petit, J., & Fabre, B. (1976). Study of an ice core to the bedrock in the accumulation zone of an alpine glacier. *J. Glaciol.*, *17*, 13–28.

Vaughan, M. J., van Wijk, K., Prior, D. J., & Bowman, M. H. (2016). Monitoring the temperature-dependent elastic and anelastic properties in isotropic polycrystalline ice using resonant ultrasound spectroscopy. *The Cryosphere*, *10*(6), 2821–2829. doi: 10.5194/tc-10-2821-2016

Wagenbach, D., Bohleber, P., & Preunkert, S. (2012). Cold, alpine ice bodies revisited: What may we learn from their impurity and isotope content? *Geografiska Annaler: Series A, Physical Geography*, *94*(2), 245–263. doi: 10.1111/j.1468-0459.2012.00461.x

Wagenbach, D., & Geis, K. (1989). The mineral dust record in a high altitude alpine glacier (colle gnifetti, swiss alps). In M. Leinen & M. Sarnthein (Eds.), *Paleoclimatology and paleometeorology: Modern and past patterns of global atmospheric transport* (pp. 543–564). Springer Netherlands. doi: 10.1007/978-94-009-0995-3_23

Wagenbach, D., Mnnich, K., Schotterer, U., & Oeschger, H. (1988). The anthropogenic impact on snow chemistry at colle gnifetti, swiss alps. *Ann. Glaciol*, *10*(183), 183–187.

Wallbrecher, E. (1986). *Tektonische und gefügeanalytische arbeitsweisen.* Ferdinand Enke Verlag Stuttgart. (geo 326 19)

Wang, Y., Kipfstuhl, S., Azuma, N., Thorsteinsson, T., & Miller, H. (2003). Ice-fabrics study in the upper 1500 m of the dome c (east antarctica) deep ice core. *Ann. Glaciol.*, *37*(1), 97–104. doi: 10.3189/172756403781816031

Wang, Y., Thorsteinsson, T., Kipfstuhl, J., Miller, H., Dahl-Jensen, D., & Shoji, H. (2002). A vertical girdle fabric in the northgrip deep ice core, north greenland. *Ann. Glaciol.*, *35*(1), 515–520.

Weikusat, I., Jansen, D., Binder, T., Eichler, J., Faria, S. H., Wilhelms, F., ... Kleiner, T. (2017). Physical analysis of an antarctic ice core – towards an integration of micro- and macrodynamics of polar ice. *Philos. Trans. R. Soc.*

London, Ser. A, *375*(2086), 20150347. doi: 10.1098/rsta.2015.0347

Weikusat, I., Kuiper, E.-J. N., Pennock, G. M., Kipfstuhl, S., & Drury, M. R. (2017). Ebsd analysis of subgrain boundaries and dislocation slip systems in antarctic and greenland ice. *Solid Earth*, *8*(5), 883–898. doi: 10.5194/se-8-883-2017

Wilhelms, F. (2005). Explaining the dielectric properties of firn as a density-and-conductivity mixed permittivity (decomp). *Geophysical Research Letters*, *32*(16). doi: 10.1029/2005GL022808

Wilson, C. J. L., Russell-Head, D. S., & Sim, H. M. (2003). The application of an automated fabric analyzer system to the textural evolution of folded ice layers in shear zones. *Ann. Glaciol.*, *37*, 7–17. doi: 10.3189/172756403781815401

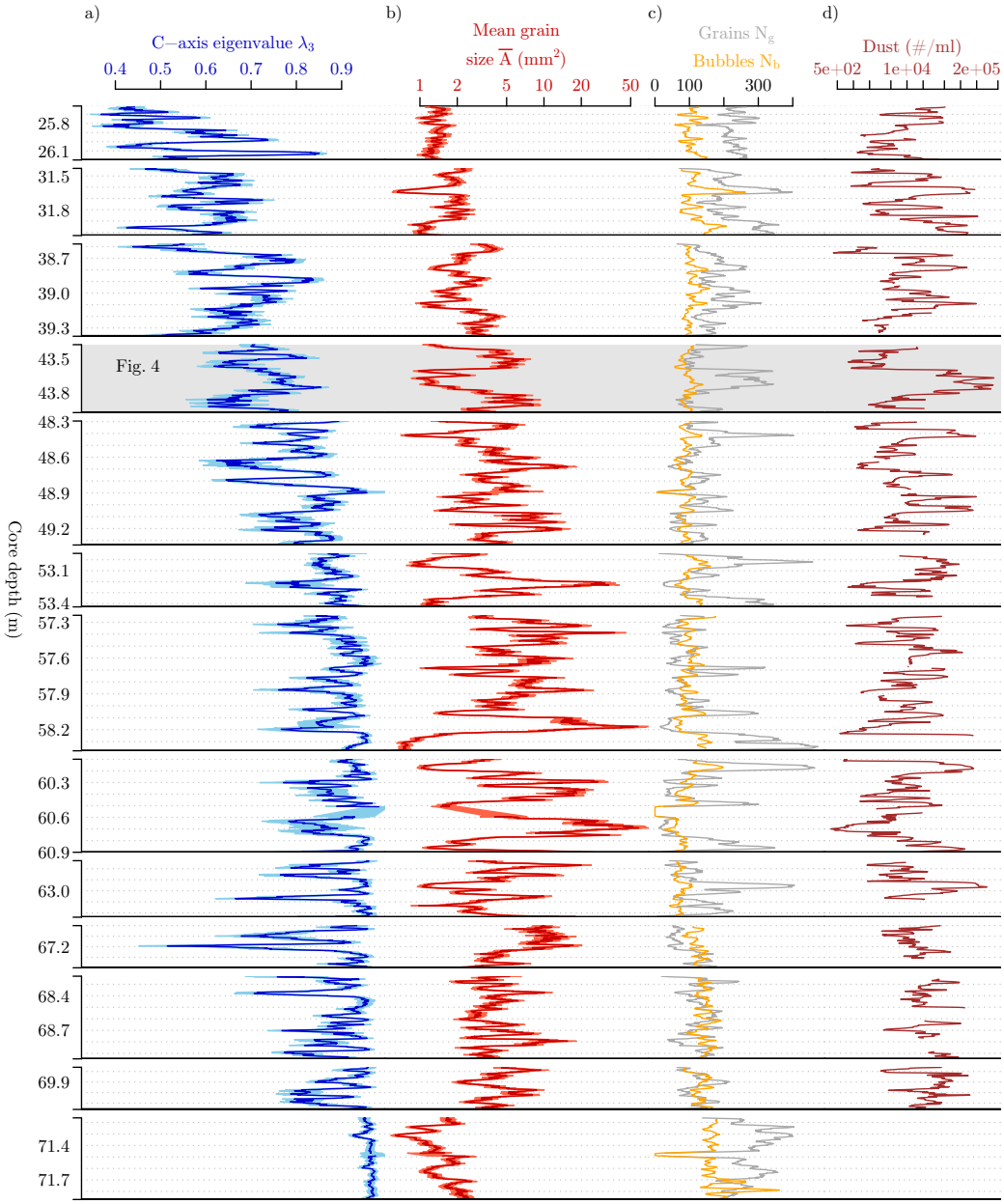

Figure 3. Physical properties parameters derived from cm-scale fabric analysis with 2 cm sliding window. The depth axis is discontinuous; horizontal black lines indicate axis breaks. a) Eigenvalue and b) mean grain size (logarithmic scale) are shown with uncertainty following Eq. 2 and 3. c) The grain number N_g is inversely related to the mean grain size and compared to the number of bubbles N_b. d) The insoluble particle concentration (referred to as "dust") from continuous flow analysis is additionally shown (logarithmic scale) for comparison. The shaded section is shown in detail in Fig. 4.

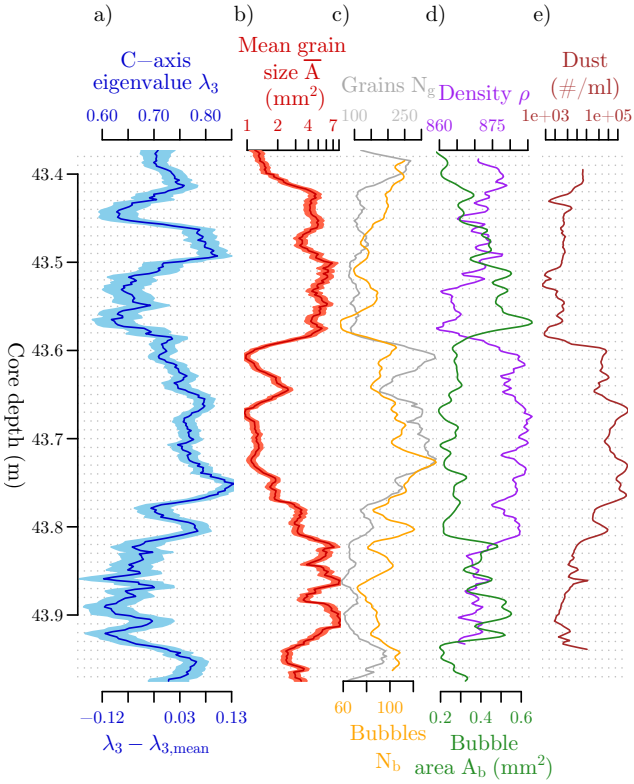

Figure 4. Excerpt from Fig. 3 showing a medium depth interval below the firn-ice transition. a) – c) as in Fig. 3. d) Density and the mean bubble area A_b are additionally shown. e) as d) in Fig. 3.

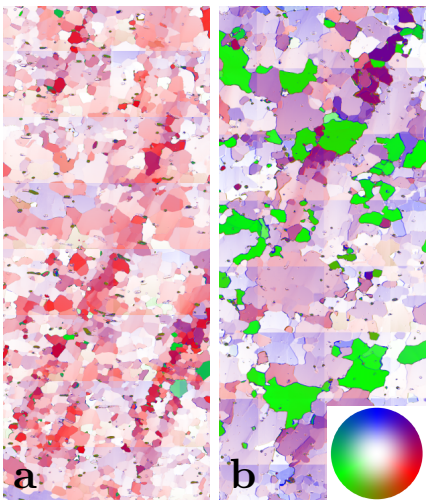

Figure 5. FA image details (3.1 × 7.5 cm^2). Left: Tilted-lattice bands (darker red) in 60.8 m depth. Right: Unconnected crystals (green) forming a second maximum inclined to the main single maximum (purple) in 70.1 m depth. The colour code indicates the c-axis orientation: the white center corresponds to a vertical orientation, parallel to the ice core axis.

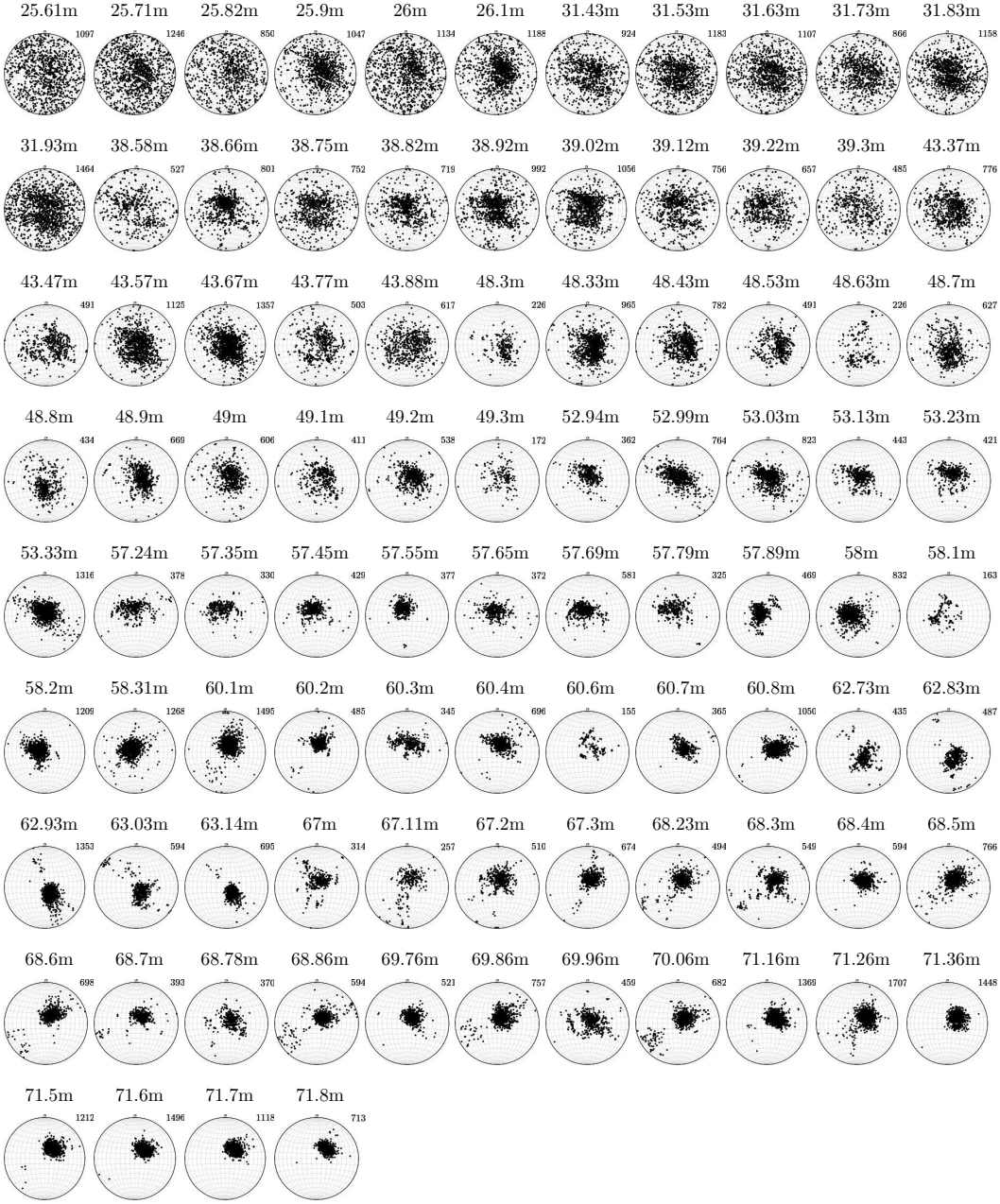

Figure B.1. Schmidt diagrams for all KCC thin sections. The number of grains is indicated on the top right of each polefigure.

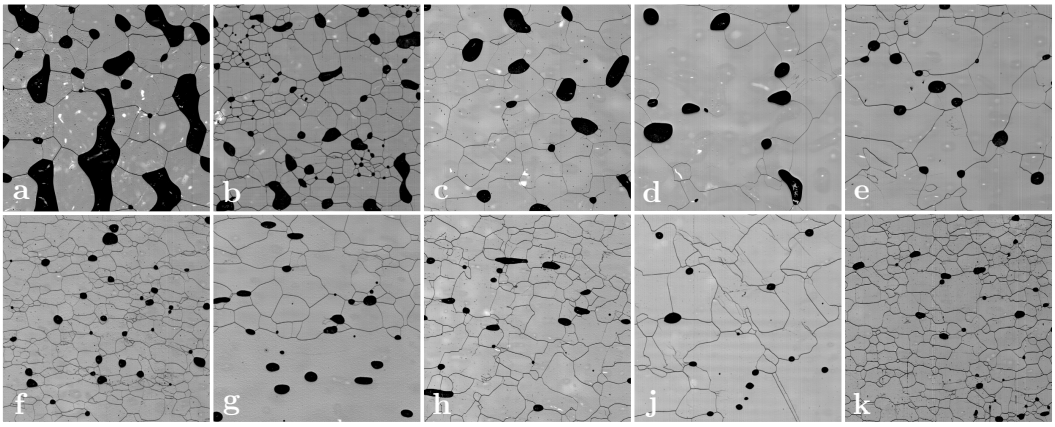

Figure B.2. Exemplary microstructure (LASM) image details (1 cm^2) from different depths of the ice core KCC. a) 25.9 m: firn. b) 31.63 m: deep firn with small-grain clusters in regions with many small bubbles. c) 38.66 m: bubble cluster just below firn-ice transition. d) Zigzagging subgrain boundaries. e) 49 m: Protruding grains and bubble alignment. f) 53.03 m: small-grain section. g) 57.35 m: small-to-large-grain transition; note that only within the large grain bubbles are not located on grain boundaries. h) 62.93 m: angular grains and inclined/elongated bubbles. j) 67.1 m: irregular grains and parallel GBs. k) 71.26 m: small-grain disribution close to bedrock.

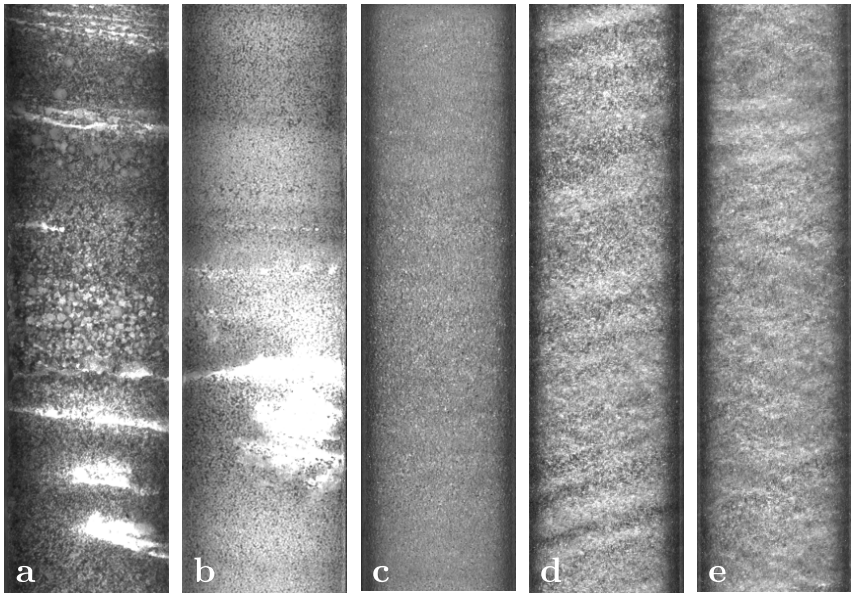

Figure B.3. Exemplary visual stratigraphy linescan images (approx. 8 × 31 cm^2) from different depths of the ice core KCC. a) 6 m depth: thin melt layers, ice lenses and coarse grains in firn. b) 24 m depth: banding and large ice lense, presumably from percolating melt in deep firn. c) 47 m depth: barely visible transitions and no discernible inclination. d) 65 m depth: inclined layers. e) 70 m depth: Layers appear very irregular.